Removing Automatically the Ambiguity in Wind Direction Retrieved from SAR Images

Maria da Conceição Proença
Department of Physics, Marine and Environmental Sciences Centre (MARE-ULisboa), Faculty of Sciences, University of Lisbon, Campo Grande, 1749-016 Lisboa, Portugal
mcproenca@fc.ul.pt

Keywords: Wind Direction, Wind Shadows, Direction Ambiguity, SAR Images, Image Processing.

Abstract: The evaluation of the wind resource in large areas to study the viability of wind farms is ideally studied using synthetic aperture radar (SAR) images in which the direction of the wind can be mapped from its effects on the water surface. Methods in use usually assume a fixed direction from a measurement for the whole image or interpolate the direction of wind fields from numerical weather models, that can be non-coincident in time with the SAR snapshot and of much less spatial resolution. The problem remains in the directional ambiguity of 180 degrees. This work presents three indexes to identify and validate initial "anchor vectors" that could be used as an aid in the complex process of remove this ambiguity, using wind shadows in the water near the coastline. These indexes consider several hypotheses to provide for local variability such as physiographic accidents, the eccentricity of the shadows and the effect of bay-shaped areas, all quantified through image processing methods. Comparing the results with the reference wind field provided by ESA for the time of acquisition of the ENVISAT-ASAR image used we could conclude that this is a promising line of work.

1 INTRODUCTION

The ambiguity in wind direction retrieval is a key problem to which there exists a very recent solution (Zhang, 2021) using support vector machine (SVM) based models, with performance still depending on sea surface wind speed. The issue of ambiguity has been addressed from time to time, although wind direction remains the most appealing problem since the 1980s (Heron, 1986), (Hildebrand, 1994); later, (Kerkmann, 1998) mentioned four different methods for removing the direction ambiguity, all involving a human operator or a trained meteorologist, one of them autonomous in the sense that no external data is needed. In the 2000s two main methods were being used to wind retrieval – those based on gradient-oriented histogram (Koch, 2004), and wavelets based (Du, 2002), (Fichaux, 2002), followed by improvements from the latter as in (Corazza, 2020), who use the Radon transform. Some adaptation of successful methods also took place, like (Horstmann, 2004) who adapts the CMOD4, originally developed for ERS-1 and 2 to ENVISAT-ASAR images with success, while (Kerbaol, 2005) uses coastal information. (Young, 2006) concludes that automatic and semi-automatic extraction of wind direction are complimentary and ensure a higher liability in wind direction retrieval from SAR images. (Koch, 2004) in the same paper mentioned above uses a semiautomatic removal of the ambiguity by combining manual selecting of unique directions on a set of subimages and automatically choosing the best aligned directions in the remaining subimages, while (Song, 2006) uses buoy data to solve the ambiguity in a comparation of two algorithms for wind speed.

The ambiguity in the direction retrieval was not an appealing subject for automation, but still seems possible to implement, at least in areas near the coast. The image processing methodology exposed here allowed the identification of anchor vectors near the shoreline that could act together with global methods to ensure the wind direction ambiguity is automatically assessed in the whole wind field, which could be useful in preliminary studies for offshore wind farms settings.

2 MATERIALS AND METHODOLOGY

The image used is a medium resolution synthetic aperture radar image that was acquired by Envisat

Proença, M.
Removing Automatically the Ambiguity in Wind Direction Retrieved from SAR Images.
In *Proceedings of the 2nd International Conference on Image Processing and Vision Engineering (IMPROVE 2022)*, pages 93-100
ISBN: 978-989-758-563-0; ISSN: 2795-4943

ASAR – Wide Swath Mode (WSM) instrument, with a nominal resolution of 150x150 m (range x azimuth), a pixel spacing of 75 m and covering 400X400 km (https://earth.esa.int) acquired over Corsica at 2007-11-13 (Figure 1-a).

To make the successive processing steps of the methodology more perceptible, we will be using the sub-image identified in red (Figure 1-b) in the ENVISAT image whenever we consider more useful that the detail is observed to illustrate the reasoning.

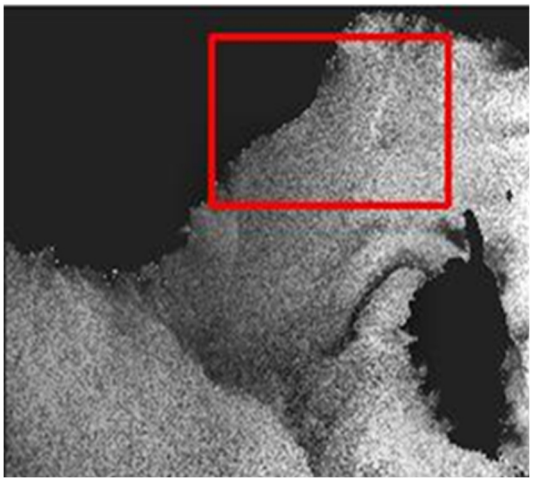

a

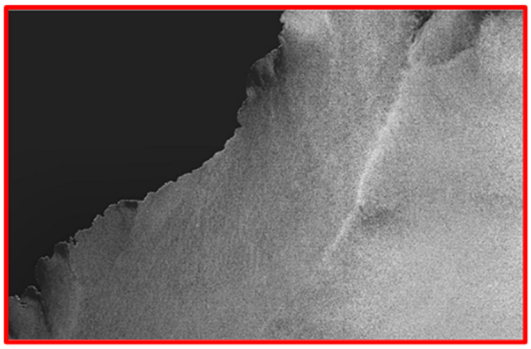

b

Figure 1: SAR image acquired by ENVISAT mission over Corsica (a) and zoom on the area which will be used to illustrate the image processing operations (b).

The first step involves calibration and computation of a land mask, and it was achieved with ESA open-source software Next ESA SAR Toolbox (NEST). A land mask is a binary image to discriminate between land and water, with two values usually 0 and 1), where we can attribute the value 1 to the subject of interest to be altered in subsequent morphological operations until we have the suitable mask to apply to the work image.

From the land mask obtained (Figure 2), a sequence of morphological and logical operations is needed to obtain a "ribbon mask". The procedure is schematically detailed in Figure 3.

Figure 2: Land mask obtained using NEST: binary image where the land is represented with the value 1 (white) and the sea area has the value 0 (black).

Using the initial land mask here represented by a white triangle in a black background (Figure 3-a), two binary images are computed: the first one by dilation, a morphological operation that enlarge the areas with value 1 presented in white (Pratt, 2001) to obtain a new mask (Figure 3-b), and the second one by inversion: the value 1 in the initial image becomes 0 and vice-versa (Figure 3-c).

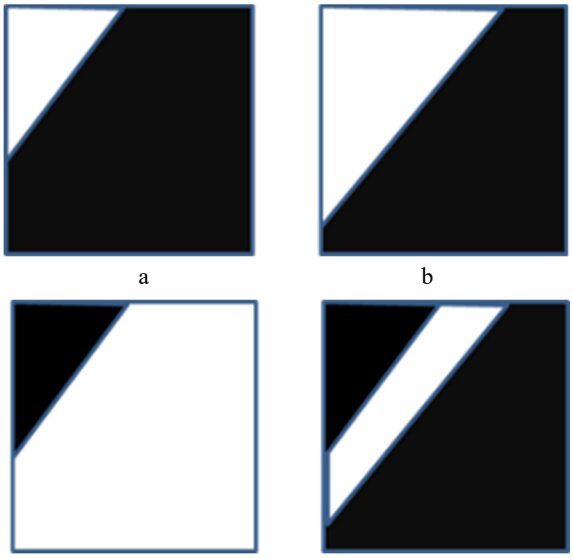

a b c d

Figure 3: Schematic representation of the sequence of operations to obtain a "ribbon" mask: (a) initial land mask, (b) dilation of (a), (c) inversion or negation of (a) and (d) logical AND between (b) and (c) – only the areas where both masks have value 1 will receive a positive value.

The structural element used for dilation in the ENVISAT image was a disk of radius 25 pixel, applied successively the number of times needed to encompass all the area containing shadows – to automatize this step, a maximum width for the mask should be assessed from a bigger dataset of images of the same sensor.

When those masks (Figure 3-b and c) are combined by a logical AND operation, the result is a "ribbon mask" (Figure 3-d).

With the new mask a corridor near the coastline can be isolated (Figure 4-a), where the wind shadows are now visible as dark spots near the shoreline (Figure 4-b).

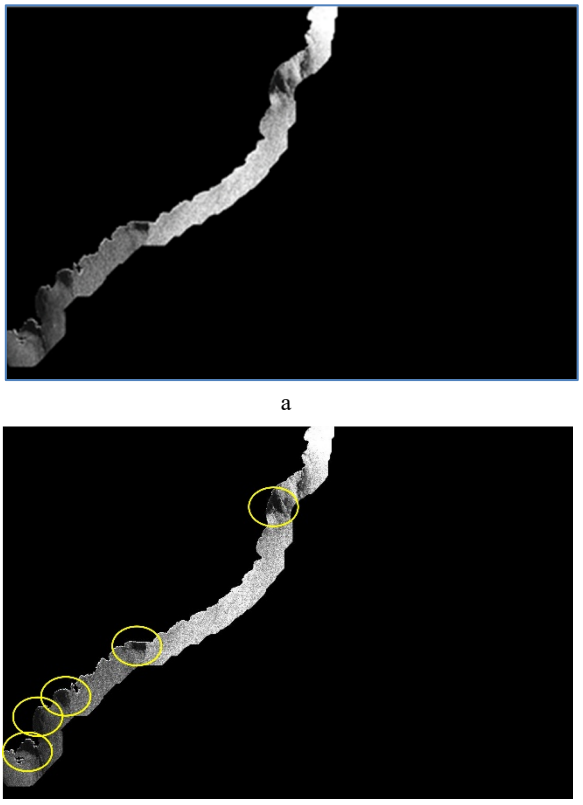

a

b

Figure 4: The "ribbon" mask is applied to the original image (a), isolating the area of water near the shoreline, where wind shadows are apparent (b).

Next step is to isolate the shadows as individual objects, which is made by thresholding the image (Figure 5-a), giving the value 1 to the pixels that are between the thresholds 0 (corresponding to the area masked) and an appropriate radiometric level, that will depend on the image codification – pixels in 16 bits images are in the range [0, 65 535], while in 8 bits images only 256 levels are possible, in the range [0, 255]. The threshold is computed using the subset of pixels belonging to the corridor and assigned to the average less two standard deviations of the intensities present.

Once the threshold is applied to the image, the resulting binary image is ready for the morphological operations needed to consolidate each shadow, that will consist in a sequence of dilation followed by erosion with the same structuring element, usually called closing (Figure 5-b), achieved with a smaller structural element to preserve the form - here a disk of radius 11.

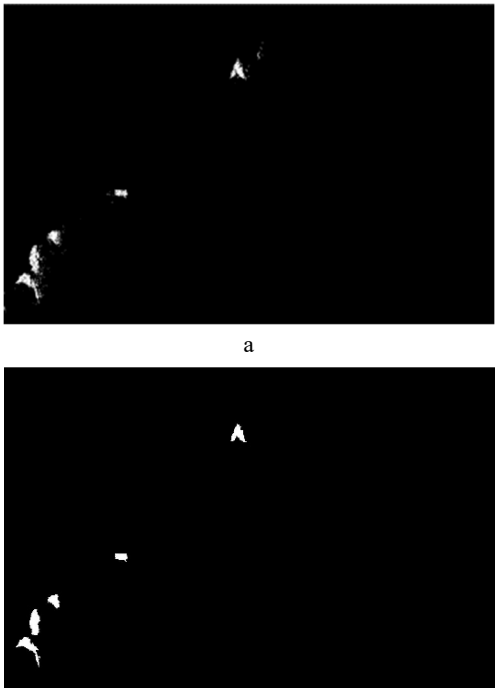

a

b

Figure 5: Candidates for wind shadows isolated by intensity thresholding (a) and consolidated using morphological operations (b).

After shadow localization, we looked for the digital elevation model (from SRTM, characterized below) to analyse each shadow and its immediate neighbourhood on land, to determine its credibility as a wind shadow (Figure 6). Three validation criteria are proposed: a bay factor, an abrupt cliff analysis and the shadow eccentricity, detailed and evaluated in the next section.

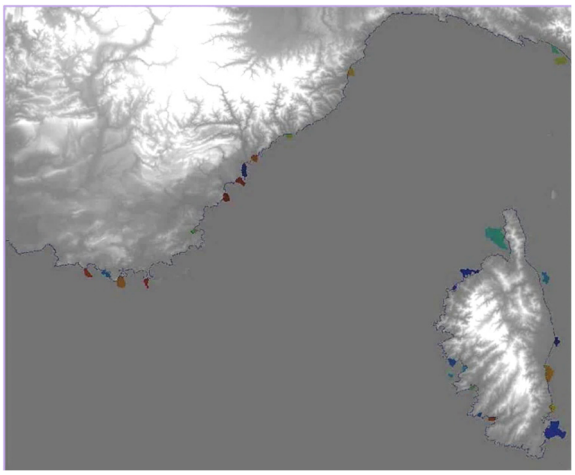

Figure 6: The candidates to wind shadows in different colours and the digital elevation model on land side.

3 VALIDATION CRITERIA

The criteria proposed for validation of the wind shadows as such are not exhaustive but worked in the range of conditions present in the image and can be applied to any similar coastline, as the three are based in common physiographic and natural effects.

3.1 Bay Factor

The rationale for the Bay factor sits in the fact that an open bay will not provoke a wind shadow, while a more closed bay will usually induce an area of shadow in the near water.

This was transformed in a quantitative index using the quotient between the number of pixels that constitute the bay envelope and the number of pixels belonging to the shadow envelope, schematically identified in Figure 7.

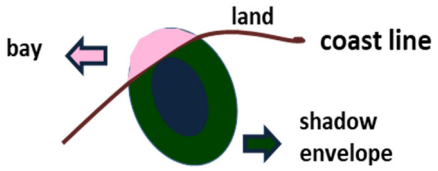

Figure 7: Definition of the pixels forming the bay envelope in pink in the land side, and the pixels belonging to the shadow envelope, in green, in turn of the blue shadow over the water.

The Bay factor computed this way (eq. 1) will be bigger for a closed bay, and low for an open bay.

$$\text{Bay factor} = \frac{\sum_{i,j \in bay} n(i,j)}{\sum_{i,j \in shadEnvelope} n(i,j)} \quad (1)$$

Examples of the values obtained for different forms of bays with this definition and the shadows previously processed are shown in Figure 8.

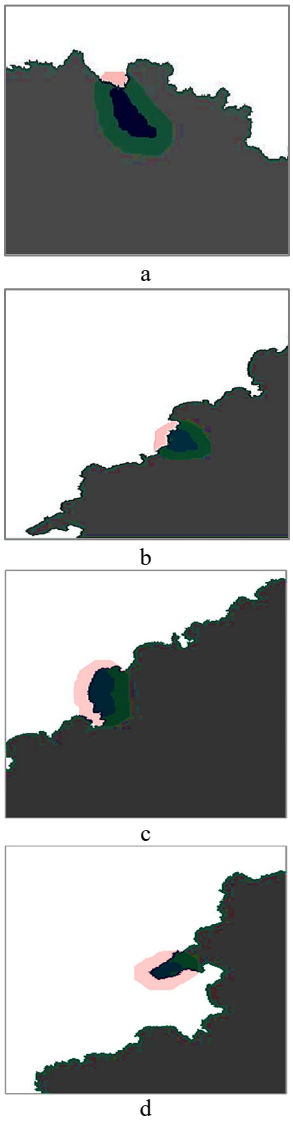

Figure 8: Examples of shadows and bays present in the image. Land is white and water is grey, and the bay and shadow envelopes follow the colour code in Figure 7. The values for the bay factor are 0.09 (a), 0.28 (b), 0.50 (c) and 0.79 (d).

A very closed bay such as the one in Figure 8-c will have a high Bay factor, but this configuration probably is enough cause for a calm water, observed as shadow in a SAR image, so shadows scoring high Bay factors will not be considered wind shadows.

3.2 Abrupt Cliff Index

The altimetry came from the digital elevation data (DEM) obtained by the Shuttle Radar Topography Mission (SRTM), an international project spearheaded by the U.S. National Geospatial-Intelligence Agency (NGA) and the U.S. National Aeronautics and Space Administration (NASA). The project covered more than 80% of the Earth's solid surface during a 11-day mission of the Space Shuttle Endeavour in February 2000. The SRTM data is available as 3 arc second (approx. 90 m ground resolution) and has a vertical error reported to be less than 16 m (https://www.usgs.gov).

This digital elevation model was used to compute the local gradient near each shadow. A flat area will have a low local gradient, and a steepest area will have a higher value (Figure 9).

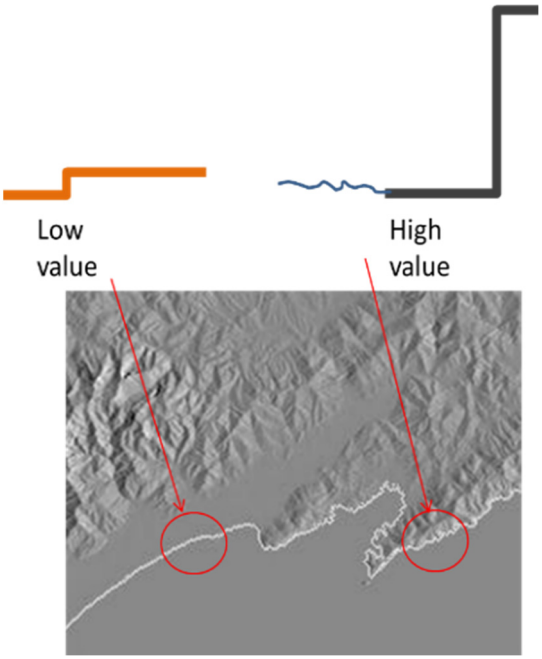

Figure 9: The flat area on the left will have a low value for the local gradient while the abrupt cliffs on the right will have a high gradient.

The cliff index is computed considering the local elevation from the DEM (Figure 10-a), its gradient (Figure 10-b), and the absolute value of this gradient (Figure 10-c). The roughness of the terrain becomes more apparent with these operations.

The ACliff index is the sum of the pixels belonging to the seashore shadow track (sst) in the image containing the absolute value of the gradient of the elevation (eq. 2).

$$\text{ACliff} = \sum_{i,j \in \text{sst}} \text{abs}(\text{grad}(\text{elevation})) \qquad (2)$$

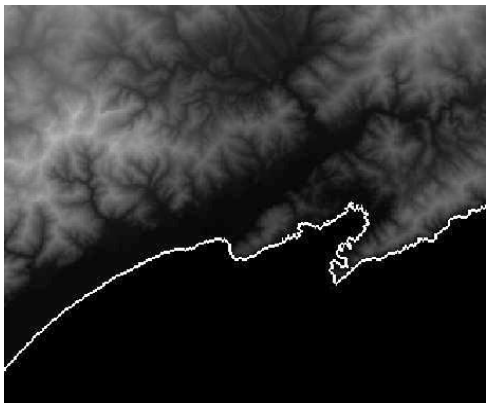

a

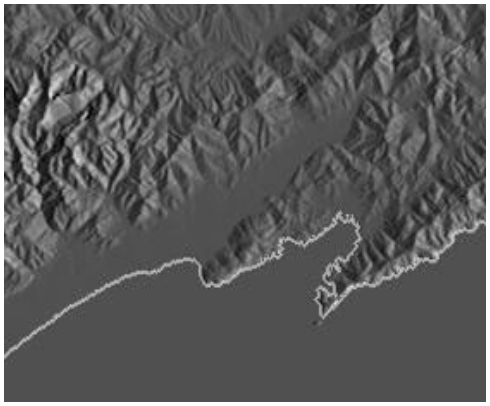

b

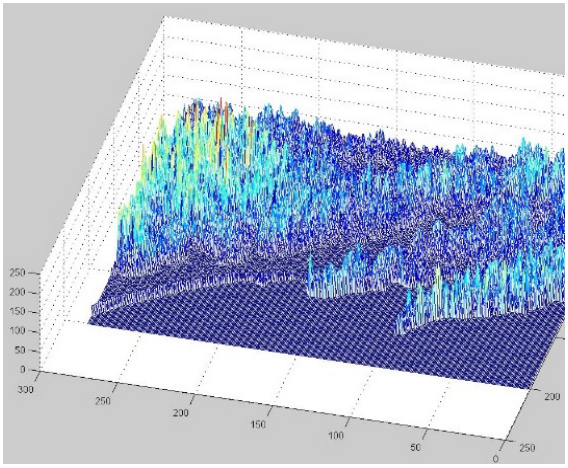

c

Figure 10: The sequence of images needed to compute the Abrupt Cliff index: the local elevation from the DEM (a), the gradient of the local elevation (b) and its absolute value (c).

As the terrain becomes steeper, the abrupt cliff index increases. When a shadow is near a flat area (Figure 11-a), the cliff index will be low, and will increase as the terrain roughness increases.

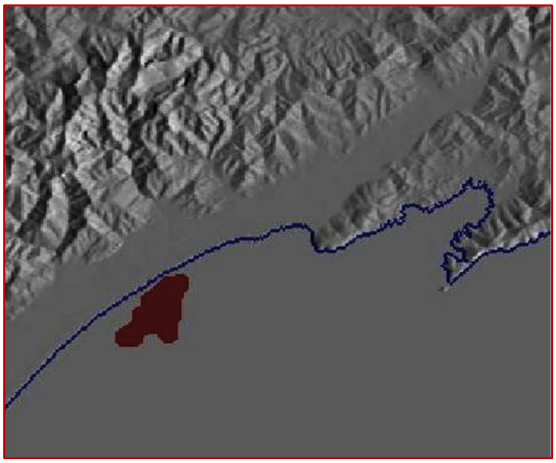

a

b

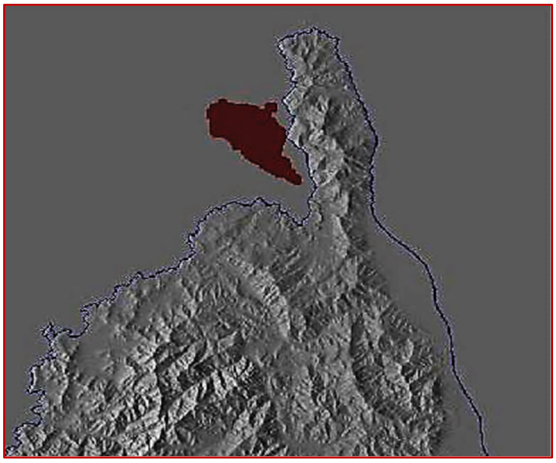

c

Figure 11: Examples of three shadows (red) near terrain with different characteristic – the CliffIndex is 1.1 for flat terrain (a), 4.8 for the shadow near median elevation (b), and 11.4 for the shadow near abrupt cliffs (c).

3.3 Shadow Eccentricity

The last indicator we consider for the localization of wind shadows is the eccentricity, computed as the eccentricity of the ellipsoid enveloping the shadow, as demonstrated in Figure 12.

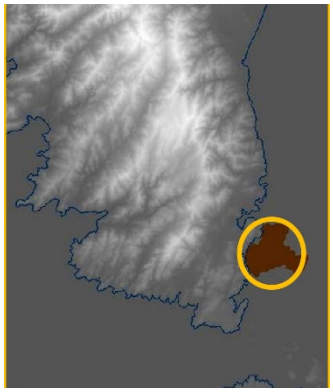

a

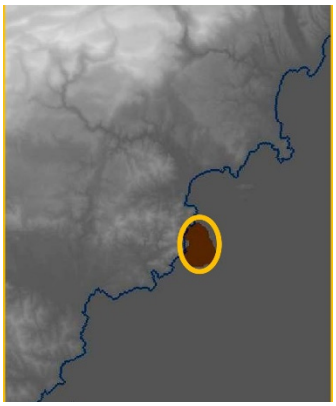

b

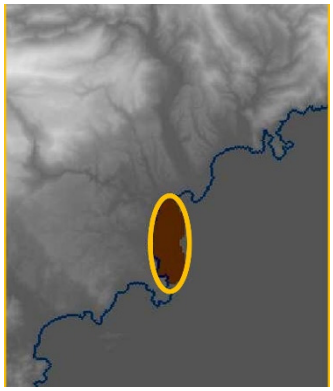

c

Figure 12: Three shadows with different eccentricity values associated: a) 0.49, b) 0.69 and c) 0.93.

The eccentricity of the ellipsoid is computed as the square root of the difference between the squared values of the lengths of the semi-major axis (a) and semi-minor axis (b) divided by the first (eq. 3).

$$\text{Eccentricity} = \frac{\sqrt{a^2 - b^2}}{a} \quad (3)$$

The information needed is the direction of the anchor vectors, that will be established from the centre of the shadows accepted (end point for the vector) and the nearest point in the coastline, considering the extension in contact with the ellipsoid enveloping the shadow (initial point for the vector). The magnitude of these vectors will be dependent of the wind field local intensity, and is usually computed automatically (Rufenach, 1998) since late 90's.

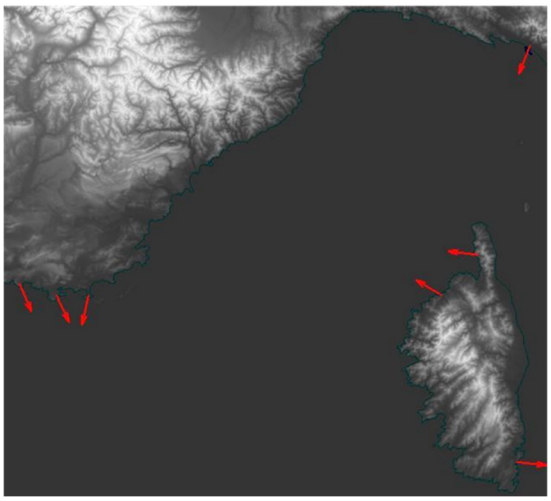

a

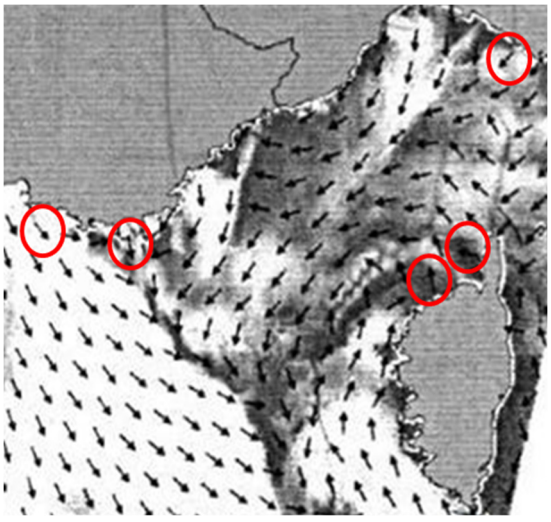

b

Figure 13: The seven anchor vectors built from the wind shadows in the SAR image (a) and the reference wind field for that date (b).

With these tree indicators, we build a criterion to accept/reject each candidate shadow as a trustful wind shadow, with a rationale including a high Cliff index to identify abrupt cliffs in the proximity of each shadow that can be the leading cause of the wind shadow, a low Bay factor to eliminate shadows in almost enclosed bay areas, and the eccentricity of the ellipses to refine admissible shadows and find the line-of-sight in the direction of the shadow to give an orientation for the anchor vector.

All these criteria and previous location of areas of interest can be automatically implemented in a single procedure, avoiding external data and human curation with inherent subjectivity. To do so, the estimation of the areas containing shadows can be done with a fixed maximum width for the ribbon mask.

From the 28 shadow candidates, only 7 verify the criteria (Figure 13-a).

Considering the positioning of the seven vectors obtained from the wind shadows and comparing with the wind vectors in approximately the same positions in the reference wind field provided by ESA for that date (Figure 13-b), we can see the orientation of the seven vectors agree in a reasonable extend with the local orientation of the wind field.

4 CONCLUSIONS

Wind field monitoring is especially important in the preliminary phase to select among the best locations for wind farms and becomes more difficult when offshore wind farms are the goal.

This case study intended to show that SAR images allow to directly extract sets of vectors near the coastline that could be used to unwrap the wind direction ambiguity in large areas automatically, complementing the wind direction retrieval that is already automatized, with a reasonable confidence.

With this kind of procedure, all the operations for wind retrieval offshore could be completed without the need of in-situ data (buoy or other external data), directly from the remote sensed images.

ACKNOWLEDGEMENTS

Envisat-ASAR image and reference wind field were both courtesy of Alexis Mouche, with CLS at the time.

REFERENCES

Zhang, Y., Chen, X., Meng, W., Yin, J., Han, Y., Hong, Z., Yang, S. (2021). Wind Direction Retrieval Using Support Vector Machine from CYGNSS Sea Surface Data. In *Remote Sens. 2021, 13, 4451.*

Heron, M., Rose, R. (1986) On the application of HF ocean radar to the observation of temporal and spatial changes in wind direction. In *IEEE J. Ocean. Eng*. 11(2), pp. 210-218.

Hildebrand, P.H. (1994) Estimation of sea-surface winds using backscatter cross-section measurements from airborne research weather radar. In *IEEE Trans. Geosci. Remote Sens*. *32*, 110–117.

Koch, W. (2004) Directional analysis of SAR images aiming at wind direction. In *IEEE Trans. Geosci. Remote Sens.* 42, pp. 702–710.

Du, Y., Vachon, P. W., Wolfe, J. (2002) Wind direction Estimation from SAR images of the Ocean Using Wavelet Analysis. In *Can. J. Remote Sens*. 28, pp. 498-509.

Fichaux, N., Ranchin, T. (2002) Combined extraction of high spatial resolution wind speed and wind direction from SAR images: A new approach using wavelet transform. In Can. J. Remote Sens. 28, pp. 510–516.

Corazza, A., Khenchaf, A., Comblet, F. (2020) Assessment of Wind Direction Estimation Methods from SAR Images. In *Remote Sens.* 12.

Horstmann, J., Koch, W., Lehner, S. (2004). Ocean wind fields retrieved from the advanced synthetic aperture radar aboard ENVISAT. Ocean Dynamics, 54 (6) :570-576.

Kerbaol, V., Collard, F. (2005). SAR-derived coastal and marine applications: From research to operational products. In *Ieee Journal Of Oceanic Engineering, 30 (3)*, pp. 472-486.

Young, G. S., Sikora, T. D., Winstead, N.S. (2006) Manual and Semiautomated Wind Direction Editing for Use in the Generation of Synthetic Aperture Radar Wind Speed Imagery, *J. Applied Meteor. and Climatology, 46,* pp. 776-790.

Song, G., Hou, Y., He, Y. (2006) Comparaison of two wind algorithms of ENVISAT ASAR at high wind, Chin. *J. of Oceanology and Limnology,* 24(1), pp. 92-96.

Kerkmann, J. (1998) Review on ScatterometerWinds, EUMETSAT Tchn. Memorandum N.3, Chap. 6.

https://earth.esa.int/ Available online: ASAR Products Information - Earth Online (esa.int), (accessed on 07/11/2021).

W. K. Pratt (2001) Digital image processing. Ed. J. Wiley & Sons, 3rd edition.

https://www.usgs.gov Available online: USGS EROS Archive - Digital Elevation - SRTM Mission Summary | U.S. Geological Survey, (accessed on 07/11/2021).

Rufenach, C. (1998) Comparison of Four ERS-1 Scatterometer Wind Retrieval Algorithms with Buoy Measurements, *J. Atm and Oceanic Technology,* 15, pp. 304-313.